WAVES IN THE MAGNETIZED SOLAR ATMOSPHERE. I. BASIC PROCESSES AND INTERNETWORK OSCILLATIONS

C. S. ROSENTHAL,[1] T. J. BOGDAN,[2] M. CARLSSON,[1] S. B. F. DORCH,[3] V. HANSTEEN,[1] S. W. MCINTOSH,[2] A. MCMURRY,[1] Å. NORDLUND,[4] AND R. F. STEIN[5]

ABSTRACT

We have modeled numerically the propagation of waves through magnetic structures in a stratified atmosphere. We first simulate the propagation of waves through a number of simple, exemplary field geometries in order to obtain a better insight into the effect of differing field structures on the wave speeds, amplitudes, polarizations, direction of propagation, etc., with a view to understanding the wide variety of wavelike and oscillatory processes observed in the solar atmosphere. As a particular example, we then apply the method to oscillations in the chromospheric network and internetwork. We find that in regions where the field is significantly inclined to the vertical, refraction by the rapidly increasing phase speed of the fast modes results in total internal reflection of the waves at a surface whose altitude is highly variable. We conjecture a relationship between this phenomenon and the observed spatio-temporal intermittancy of the oscillations. By contrast, in regions where the field is close to vertical, the waves continue to propagate upward, channeled along the field lines but otherwise largely unaffected by the field.

Subject headings: MHD — Sun: chromosphere — Sun: magnetic fields — Sun: oscillations

1. INTRODUCTION

The influential papers of Biermann (1948), Schwarzschild (1948), Thomas (1948), and Osterbrock (1961) focused the attention of a generation of astrophysicists on the problem of wave propagation in magnetized stellar atmospheres. The initial flurry of activity attempted to determine the efficacy of convection-generated waves in transporting and depositing mechanical energy in the overlying chromospheric and coronal plasmas.

The question remains unanswered despite continuing efforts over the last half a century. In large part, this can be traced to the complicated mathematical description of the underlying physical processes that bear on wave propagation in realistic magnetoatmospheres. The principal players are magnetohydrodynamics (MHD), radiative transfer (RT), and nonequilibrium thermodynamics (non-LTE), and their activities are described by a coupled system of nonlinear partial differential equations (PDEs) in seven independent variables (three space and one time coordinate, plus the three components of a photon's momentum). Analytic solutions are out of the question. Direct numerical solutions present a very difficult undertaking from both conceptual and computational perspectives.

Observationally based efforts to settle the "wave-heating" question have fared no better than their theoretical counterparts. The last two decades have witnessed many first-time detections of waves and oscillations in a wide variety of solar structures and atmospheric layers. Oscillatory motions are present in sunspots, prominences, coronal and chromospheric loops, in the emission-line corona, in the network and internetwork photosphere, in the deep solar interior, and in the distant solar wind. We detect these fluctuations through their characteristic imprints upon emergent Stokes profiles, from the radio to the extreme-ultraviolet wavelengths of the spectrum. However, an accurate interpretation of these data in terms of wave energy and momentum flux densities remains subject to the grave uncertainties that invariably attend ill-posed inverse problems.

Significant progress has recently been achieved in understanding wave propagation in nonmagnetic atmospheres. At the heart of this success is a novel data-assimilation strategy that combines numerical simulations with high-precision spectroscopic observations having sufficient spatial and temporal sampling cadences. Carlsson & Stein (1997) have employed this strategy with remarkable success in the study of the Ca II H and K grain phenomenon. Their numerical code takes full account of RT and non-LTE atomic level populations, while faithfully evolving the hydrodynamics. The simulation was driven at the lower atmospheric boundary with Doppler velocities observed in the photospheric Fe I 396.68 line present in the broad wings of the Ca II H resonance line (Lites, Rutten, & Kalkofen 1993). The resulting temporal behavior of the Ca II H_{2V}, which was also observed by Lites et al. (1993), was found to be in remarkable agreement with that synthesized from the driven simulation. This success allowed Carlsson & Stein (1997) to develop a physically satisfying explanation of how the radiation interacts with the hydrodynamics to produce the observed bright-grain behavior in the core of the Ca II H and K resonance lines.

The Carlsson and Stein study was made tractable by assuming translational invariance in the two lateral spatial coordinates and by ignoring magnetic effects. Their success, while remarkable, was also in some sense limited to a specific physical process where their approximations are justified a posteriori. With this paper, we report on a long-term ongoing research initiative to extend the Carlsson and Stein approach to include MHD effects and to permit nontrivial

[1] Institute of Theoretical Astrophysics, University of Oslo, Box 1029, N-0315 Blindern, Oslo, Norway.

[2] HAO/NCAR, Box 3000, Boulder, Colorado, CO 80307-3000.

[3] The Royal Swedish Academy of Sciences, Stockholm Observatory, SE-133 36 Saltsjöbaden, Sweden.

[4] NBIfAFG, Københavns Universitet, Juliane Maries Vej 30, DK-2100 København Ø, Denmark.

[5] Department of Physics and Astronomy, Michigan State University, East Lansing, MI 48824.

variations in the lateral spatial coordinates. By relaxing these assumptions, we hope to extend the physical understanding developed for the Ca II H and K bright grain phenomenon to other dynamic processes in the solar atmosphere. An enhanced capability to treat a wide variety of atmospheric dynamics brings us an important step closer to answering the "wave-heating" question posed at the start of this discussion.

As a first step toward this goal, we report here on two-dimensional simulations of waves in stratified but non-radiating magnetoatmospheres. To limit the nonessential complications, the imposed magnetic field is potential (i.e., current-free), and the atmosphere is isothermal. We solve the compressible MHD equations subject to a constant gravitational acceleration but restrict the motions to be isentropic. In subsequent efforts we shall systematically eliminate these limitations in keeping with our scientific objectives.

The work of Shibata (1983) is one of the few previous solutions of a fully two-dimensional nonlinear magneto-acoustic wave problem in a stratified atmosphere. Starting with an initially uniformly magnetized atmosphere, he introduces a strong localized pressure pulse, which excites fast and slow magnetoacoustic waves as well as vortical motion at the site of the initial pressure pulse. More recently, Cargill, Spicer, & Zalesak (1997) found numerical solutions for wave propagation in geometries similar to some of those discussed here. However, while their technique is certainly applicable to the problems discussed in this paper, they chose instead to concentrate on the predominantly Alfvénic solutions obtained when the system is driven by motions in the invariant direction, whereas we are here primarily concerned with the predominantly magneto-acoustic solutions that are relevant when driving is in the noninvariant directions.

The astrophysical focus of this paper is on how the magnetic field topology of the network/internetwork regions affects the propagation of waves generated at the atmospheric base. The drivers used here are not taken from observations but are prescribed analytic functions of time. Since the RT and non-LTE aspects of the simulation are not in effect here, there is little utility in pursuing the full data assimilation strategy. Rather, the emphasis of this paper is to gain a basic familiarity with how the magnetic effects come into play.

The methods used are described in § 2, and this is followed in § 3 by a brief review of the relevant physics. In § 4 we discuss results from exemplary models corresponding to simplified field geometries. As an application to a more realistic field geometry, we discuss the case of internetwork and network oscillations in §§ 5 and 6. Our conclusions are presented in § 7.

2. NUMERICAL METHOD

We solve the equations of nonlinear, compressible MHD in two dimensions using the (three-dimensional) numerical code described in Dorch & Nordlund (1998), Mackay & Galsgaard (2001), and in more detail by Nordlund & Galsgaard.[6] In short, the code functions as follows: the variables are represented on staggered meshes, such that the density ρ and the internal energy e are volume-centered, the magnetic field components B and the momentum densities ρu are

[6] See http://www.astro.ku.dk/~kg.

face-centered, while the electric field E and the current J are edge-centered. A sixth-order accurate method involving the three nearest neighbor points on each side is used for determining the partial spatial derivatives. In the cases where variables are needed at positions other than their defined positions, a fifth-order interpolation scheme is used. The equations are stepped forward in time using the explicit third-order predictor-corrector procedure by Hyman (1979), modified for variable time steps. In order to suppress numerical noise, high-order artificial diffusion is added in both the form of a viscosity and the form of a magnetic diffusivity.

The code has been tested on a wide range of standard test problems such as the hydrodynamic Sod shock tube (Sod 1978), the Orszag-Tang vortex system (Orszag & Tang 1979), and the Dai-Woodward two-dimensional MHD shock (Dai & Woodward 1998). In all cases the code performed competitively against other MHD codes described in the literature.

We have implemented boundary conditions that are designed, so far as is practical, to allow waves to be injected at the lower boundary of the computational domain and to propagate out through the upper boundary. For the hydrodynamic variables (the vertical velocity, density, and pressure) we implement characteristic boundary conditions in the manner described by Korevaar (1989). For the horizontal velocity and magnetic field we implement the same method applied to characteristics corresponding to incoming and outgoing shear modes traveling at the Alfvén speed. The vertical component of the field at the boundary is then allowed to vary freely according to the induction equation. Thus, we do not treat the case of fully coupled MHD waves but instead assume that the waves crossing the boundary can be separated into longitudinal waves traveling at the sound speed and transverse waves traveling at the Alfvén speed. In the horizontal direction all variables are periodic.

The system is driven by forcing at the lower boundary. A wide variety of different driving mechanisms can be implemented. For the exemplary models we describe in § 4 we consider both horizontal driving, in which the whole lower boundary is shaken horizontally at a fixed frequency, and vertical driving, in which the whole lower boundary is shaken vertically at a fixed frequency. In the simulations of waves in the internetwork and network (§§ 5 and 6) the oscillations are forced with vertically moving horizontally localized pistons. This localized forcing provides a clearer picture of the wave dynamics and may also be a better model of the real solar forcing of such oscillations by collapsing granules (Skartlien, Stein, & Nordlund 2000).

3. A PHYSICS PROLOGUE

3.1. Uniformly Magnetized Fluid

The interpretation and identification of propagating waves in general magnetoatmospheres is best effected through a working knowledge of MHD wave properties in idealized equilibria possessing a high degree of symmetry. In this section we shall briefly recount the essential results of these pedagogical examples and also establish the terminology that will be adapted to general magnetohydrostatic equilibria which lack symmetries.

The most basic example is that of wave motions in a homogeneous, compressible, ideal fluid threaded by a uniform magnetic field. Without loss of generality, we may

assume a common factor $\exp[i(\mathbf{k} \cdot \mathbf{x} - \omega t)]$ for all fluctuations. The symmetries permit one to align the magnetic field with the z-axis, and to restrict the wavevector $\mathbf{k}$ to lie within the x-z plane. Let φ denote the angle between $\mathbf{B}$ and $\mathbf{k}$. The elimination of the pressure and magnetic field fluctuations in favor of the (Lagrangean) displacement of a fluid element ξ, and the replacement of derivatives by wavevector and frequency multiplications, results in a set of three linear homogeneous equations in the three (unknown) components of the fluid displacement vector, ξ_x, ξ_y, ξ_z:

Nontrivial solutions exist only for specific choices of the phase speed $v = \omega/k$, which are equivalent to the eigenvalues of the associated 3×3 matrix. The eigenvalues may be ordered in decreasing magnitude as follows,

$$v_+^2 = \tfrac{1}{2}\left(a^2 + c^2 + \sqrt{a^4 + c^4 - 2a^2c^2 \cos 2\varphi}\right), \quad (1)$$

$$v_0^2 = a^2\cos^2\varphi, \quad (2)$$

$$v_-^2 = \tfrac{1}{2}\left(a^2 + c^2 - \sqrt{a^4 + c^4 - 2a^2c^2 \cos 2\varphi}\right), \quad (3)$$

where $a \equiv B/(4\pi\rho)^{1/2}$ is the Alfvén speed and $c \equiv (\gamma p/\rho)^{1/2}$ is the (adiabatic) sound speed. To each of these three eigenvalues there corresponds a displacement eigenvector. These eigenvectors are mutually orthogonal, and they satisfy $\hat{e}_- \times \hat{e}_0 = \hat{e}_+$, for $\varphi \in (0,\tfrac{1}{2}\pi)$. The orientation of our Cartesian coordinate system ensures that $\hat{e}_0 = \hat{e}_y$. Thus, $\hat{e}_\pm$, like the wavevector and the background magnetic field, both lie within the x-z plane. Let ψ denote the angle between $\mathbf{B}$ and $\hat{e}_+$, then

$$\tan\psi = \frac{c^2 \sin 2\varphi}{c^2 \cos 2\varphi - a^2 + \sqrt{a^4 + c^4 - 2a^2c^2 \cos 2\varphi}}. \quad (4)$$

It is conventional to call the "plus" solution the *fast-mode* wave, the "minus" solution the *slow-mode* wave, and the "0" solution the *intermediate-mode* or the *Alfvén* wave. According to the above equation, for $a \geq 2c$, $\psi \lesssim \pi/2$, while for $c \geq 2a$, $\psi \gtrsim \varphi$. For high magnetic field strengths, the fast-mode displacement is perpendicular to $\mathbf{B}$ irrespective of the propagation direction. For weak magnetic fields, the fast-mode displacement is nearly aligned with the wavevector irrespective of the field direction.[7] In this latter case, the fast mode is *longitudinally polarized*, while the slow mode is *transversely polarized*. Notice that in the strong field limit, the fast mode exhibits transverse polarization for propagation along the background magnetic field, but it switches to longitudinal polarization for propagation across the magnetic field. Should the sound speed and the Alfvén speeds be comparable, then one finds that $\psi \approx (\pi/4) + \tfrac{1}{2}\varphi$.

Finally, we point out that the gas pressure and magnetic pressure $(\mathbf{B} \cdot \mathbf{B}'/4\pi)$ fluctuations are in phase and add constructively for the fast mode. For the slow mode they are out of phase and tend to cancel. For the intermediate mode they both vanish identically.

3.2. *Uniformly Magnetized Atmosphere*

In the presence of gravitational and/or thermal stratification, the situation described in the previous subsection must be modified to account for the restoring force owing to the buoyancy of a displaced parcel of fluid, and to encompass the nontrivial variation of the atmosphere along the stratification direction.

To be definite, suppose that the gravitational acceleration and the direction of stratification are both aligned with the (negative) z-axis of a Cartesian coordinate system. The uniform magnetic field is taken to lie in the x-z plane and to make an angle $\theta \in [0,(\pi/2)]$ with respect to the unit vector $\hat{e}_z$. The arbitrary stratification in the z-direction restricts the Fourier analysis to the x-y plane (note that, unlike the previous case, the field has a component in the x direction, so the x and y directions are not equivalent). The (lateral) wavevector must also lie in this plane, and we suppose it makes an angle $\psi \in (0, \pi)$ with respect to the unit vector $\hat{e}_x$.

The elementary fluctuations from which general wave motions may be constructed by superposition all carry a common factor $\exp[ik(x \cos\psi + y \sin\psi - vt)]$. The dependence upon the z-coordinate must be determined from the ensuing set of ordinary differential equations (ODEs).[8] These equations may be (and have been) written down in numerous ways—the system is equivalent to a single sixth-order ODE or a set of six coupled first-order ODEs (Thomas 1982; Zhugzhda & Dzhalilov 1984a).

This fact indicates that the three distinct MHD wave modes of the previous subsection, viz., the fast, intermediate, and slow modes, are no longer distinct. Instead, they are coupled to one another and are subject to mixing and conversion during the course of propagation. Following the convention of Thomas (1983), we shall refer to the solutions of this set of ODEs as *magnetoatmospheric waves* (MA waves).

With the exception of Zhugzhda & Dzhalilov (1984a), little attention has been given to studying the full sixth-order system. Rather, certain simplifications have been noted, and these special cases have been the subject of intense investigation. For example, the intermediate-MA (or Alfvénic) wave decouples from the remaining waves if (1) $\psi = 0, \pi$ (i.e., no variations perpendicular to the magnetic field and gravitational acceleration), (2) $\theta = 0$ (i.e., the magnetic field is aligned with the gravitational acceleration), or (3) $\theta = \psi = \pi/2$ (i.e., the magnetic field, lateral wavevector, and the gravitational acceleration are mutually orthogonal). Provided $\theta \neq \pi/2$, the remaining fast and slow MA waves remain coupled and yield a fourth-order system of ODEs. The lower degree of this system of ODEs makes the ensuing analysis more tractable and easier to interpret (e.g., Ferraro & Plumpton 1958; Weymann & Howard 1958; Zhugzhda & Dzhalilov 1982; Zhugzhda & Dzhalilov 1984b; Leroy & Schwartz 1982; Thomas & Scheuer 1982; Schwartz & Bel 1984; Zhukov 1985; Kamp 1989; Campos & Saldanha 1991; Hasan & Christensen-Dalsgaard 1992; Banerjee, Hasan, & Christensen-Dalsgaard 1995; Bogdan & Cally 1997; Cally 2001).

The oblique magnetic fields ($\theta \neq \pi/2$) have a crucial property that is not shared by their horizontal (see below) counterparts: the ratio of the sound speed to the Alfvén speed varies along every magnetic line of force. In particu-

---

[7] The slow-mode displacement is of course offset by $\pi/2$.

[8] A wavevector along the z-direction may be uniquely defined through the use of the Hilbert transform but will be found to be a complicated function of z, *and* it need not be identical for all the fluctuations associated with the wave. In the high-frequency, WKBJ limit where the definitions become uniform, this concept of course proves extremely fruitful.

lar, it is possible for field lines to have opposite ends rooted in high- and low plasma-β atmospheric layers. At these extremes, where $a \gg c$ or $c \gg a$, the general system of ODEs factors into three weakly coupled second-order ODEs, which can once again be identified with fast, intermediate, and slow MA waves. The essential physical reason for this is the large disparity between the effective wavelengths of the fast [max $(c, a)/\omega$] and slow [min $(c, a)/\omega$] modes of propagation. It is important to keep in mind that *different* decouplings pertain to the high- and low-β ends of each field line. For example, the fast MA wave in the high-β plasma is essentially a longitudinal acoustic wave, while the slow MA wave becomes one of the two transverse Alfvén waves. In the low-β plasma, the slow MA wave is a longitudinal acoustic wave that is guided along the magnetic lines of force, while the fast MA wave becomes a predominantly transverse oscillation in which magnetic tension is the principal restoring force. Between these two extremes is a mixing layer where $a \approx c$ and mode-conversion, transmission, and reflection occurs. Such $\beta \approx 1$ mixing layers also play a fundamental role in the behavior of waves in general magnetoatmospheres.

We conclude this subsection by pointing out that the horizontal magnetic field limit $\theta \to \pi/2$, is singular. Putting $\theta = \pi/2$ in the governing ODEs reduces the order of the system from 6 to 2. The second-order ODE possesses movable singularities that are not present in the sixth-order system. These are usually manifested as *critical layers*, where energy fluxes are discontinuous and fluctuations are nonanalytic in the $t \to \infty$ steady-state limit. For $\psi \neq 0$, there are generally *two* critical layers termed the *Alfvén* and *cusp* resonant layers. When the horizontal wavevector is aligned with the magnetic field ($\psi = 0$) only the cusp resonance remains, as the Alfvén waves are decoupled (Nye & Thomas 1976; Adam 1989). It is worth noting that specific magnetoatmospheres need not possess any of these critical layers (e.g., Yu 1965).

The spectacular behavior of the fluctuations in the vicinity of the critical layer(s), coupled with the implications suggested by the nonzero divergence of the wave energy flux, have prompted intense interest and investigation of the horizontal magnetic field limit (see Nye & Thomas 1976; Adam 1981, 1986, 1989, 1990; and Cally 1984) for a comprehensive mathematical analysis and, e.g., (Zhukov 1990; Rosenthal 1990; Zhukov 1997; Pintér, Čadež, & Goossens 1998; Tirry et al. 1998; Vanlommel & Goossens 1999; Pintér & Goossens 1999 for solar applications). A contradictory point of view has been proposed by Schwartz & Bel (1984), who argue that critical layers are likely to be a "red herring" from an astrophysical point of view.

4. EXEMPLARY MODEL CALCULATIONS

At the next level of complexity, we may retain the hydrostatic stratification along the z-direction but extend our attention to force-free and potential magnetic fields that are not unidirectional. This brings us to the class of MA-wave propagation problems that are the concern of this investigation.

As Wright & Evans (1991) point out, the fluctuating Lorentz force is generally best described in an orthogonal coordinate system fitted to the equilibrium magnetic field (see Dungey 1969; Murata 1986; Cross 1988a, 1988b; Wright 1990, 1991, 1992 and references therein). In certain

instances, for example, a dipole magnetic field, this coordinate system is readily determined. Realistic complex field topologies may only permit a local fitting, as the Euler potentials are multivalued. The governing equations are a set of coupled PDEs, but as the above-cited references describe, in very fortuitous circumstances, these PDEs may decouple. The basic requirements for this simplification are the neglect of the fluid compressibility (i.e., $c/a \to 0$) and buoyancy effects ($\omega g/c \to 0$). Even under these most favorable of circumstances, the resultant PDEs are generally not solvable in terms of ODEs through the method of separation of variables. The critical layer phenomenon may also persist in these more general circumstances, but it generally requires line-tying of the magnetic field at a rigid boundary (e.g., Goossens, Poedts, & Hermans 1985; Poedts, Hermans, & Goossens 1985; Poedts & Goossens 1987, 1988; Tirry & Goossens 1995).

The neglect of buoyancy and compressibility restoring forces is not justified for wave propagation in the solar atmosphere. Neither is reliance on eikonal methods a viable alternative (e.g., Weinberg 1962; Bazer & Hurley 1963; McKenzie 1973; Yeh 1974; Hollweg & Lilliequist 1978; Barnes 1992) for the relevant oscillation periods (10–1000 s). Accordingly, we have adopted a numerical scheme (see § 2) for solving the primitive conservation equations of mass, momentum, and energy, coupled with the magnetic induction equation.

4.1. *Basic Magnetoatmospheric State*

Throughout this paper, the plane-parallel hydrostatic atmosphere is isothermal with a scale-height, H, of 158 km and an adiabatic sound speed of 8.49 km s^{-1}. At the atmospheric base, the density and pressure are 2.60×10^{-7} gm cm^{-3} and 1.13×10^5 gm cm^{-1} s^{-2}, respectively. A constant gravitational acceleration of 2.74×10^4 cm s^{-2} is adopted, and the ratio of specific heats is set at 5/3.

With no magnetic field, the linear oscillations of this atmosphere are the familiar acoustic-gravity waves. They propagate vertically when

$$ k_\parallel^2 \equiv \frac{\omega^2 - \Omega^2}{c^2} + k^2 \left(\frac{N^2}{\omega^2} - 1 \right) \tag{5} $$

is positive (with the notation of § 3 remaining in force). For fixed horizontal wavenumber, k, propagation is always possible at sufficiently great $\omega \gg \Omega$ (acoustic waves) and sufficiently small $\omega \ll N$ (internal gravity waves) frequencies. The quantities N and Ω are the Brunt-Väisälä (also known as buoyancy) and acoustic cut-off frequencies, respectively (dimensions: rad s^{-1}). For our adopted isothermal atmosphere parameters, these characteristic frequencies (divided by 2π) are 4.19 and 4.28 mHz, respectively.

The initial background magnetic field is free of electric currents and will be translationally invariant along the y-axis in this paper. (In fact, we also set $B_y = 0$.) It can therefore be generated either from a potential Φ or from a stream-function Ψ according to $\boldsymbol{B} = \nabla \Phi = \nabla \times \Psi \hat{e}_y$. Both $\Phi(x, z)$ and $\Psi(x, z)$ are solutions of Laplace's equation; thus, a Fourier component of the potential (and stream-function) that varies as $\sin 2n\pi x/L$ decays with height as $\exp -2n\pi z/L$. Unlike the adiabatic sound speed, c, which is strictly constant, the Alfvén speed $a(x, z) = \|\nabla\Phi\|/[4\pi\rho(z)]^{1/2} = \|\nabla\Psi\|/[4\pi\rho(z)]^{1/2}$ is generally a function of *both* x and z coordinates. Consequently, the aforementioned wave-mixing layer(s), where $c = a(x, z)$ or equivalently $\beta(x, z)$

$= 2/\gamma = 1.2$, can exhibit complex topological structure. One special case deserves mention. If the potential magnetic field consists of a *single* ($n = 1$) Fourier component with $L = 4\pi H$, where H is the scale height of the isothermal atmosphere, then the Alfvén speed is also strictly constant throughout the entire atmosphere. It is then possible to assume a common factor $\exp ik(y \sin \chi + z \cos \chi - vt)$ for the fluctuations and reduce the wave propagation problem to a sixth-order ODE in the x-coordinate (Oliver et al. 1993; Čadež, Oliver, & Ballester 1996).

All our calculations are two-dimensional in the following sense. In the initial state, there is no component of **B** or **u** in the y-direction. Also the initial state is invariant in the y-direction. Driving is by specifying the displacement of the lower boundary in either the x or z direction, and the specified displacement is also invariant in the y direction. Thus, the system will be invariant in the y-direction for all times, and B_y and u_y are zero for all times.

4.2. *Open vs. Closed Field Structures*

To gain a rudimentary knowledge of MA-wave propagation in two-dimensional magnetoatmospheres, we consider a matrix of four simulations displayed in Figures 1–6 and described in Table 1. There are two equilibrium magnetic field configurations. One consists of a unipolar magnetic field that is concentrated into two intense flux slabs (Figs. 1–3), while the other has an additional weaker concentration of opposite polarity (Figs. 4–6). At the upper boundary of both equilibria, the field is essentially uniform and of the

TABLE 1
DESCRIPTION OF FIGURES 1–6

Figure	Field Configuration	Piston Type	Variables Shown
1	Open	Horizontal	$u_{\parallel}$, $u_{\perp}$
2	Open	Vertical	$u_{\parallel}$, $u_{\perp}$
3	Open	Vertical	$\rho^{1/2}u_x$, $\rho^{1/2}u_z$
4	Mixed	Horizontal	$u_{\parallel}$, $u_{\perp}$
5	Mixed	Vertical	$u_{\parallel}$, $u_{\perp}$
6	Mixed	Vertical	$\rho^{1/2}u_x$, $\rho^{1/2}u_z$

dominant polarity, consistent with the exponential decay of the $n \neq 0$ Fourier components of **B**. In the unipolar case, the uniform field is 750 G as compared with 600 G in the bipolar equilibrium. At the atmospheric base the peak field strengths are on the order of 5000 G for the unipolar example and 7000 and 1500 G, respectively, for the dominant and opposite polarity regions in the mixed polarity case.

To complement the two equilibrium field configurations, we adopt two simple forcings at the lower boundary to generate the waves. The entire lower boundary is moved sinusoidally as a whole in either the vertical (radial driving: Figs. 2, 3, 5, and 6), or horizontal (transverse driving: Figs. 1 and 4) directions. That is to say in the former case we specify u_z and set $u_x = 0$, and in the latter case we specify u_x and set $u_z = 0$. In either case, the oscillation frequency is 42 mHz (period = 23.8 s). For radial driving we adopt a peak veloc-
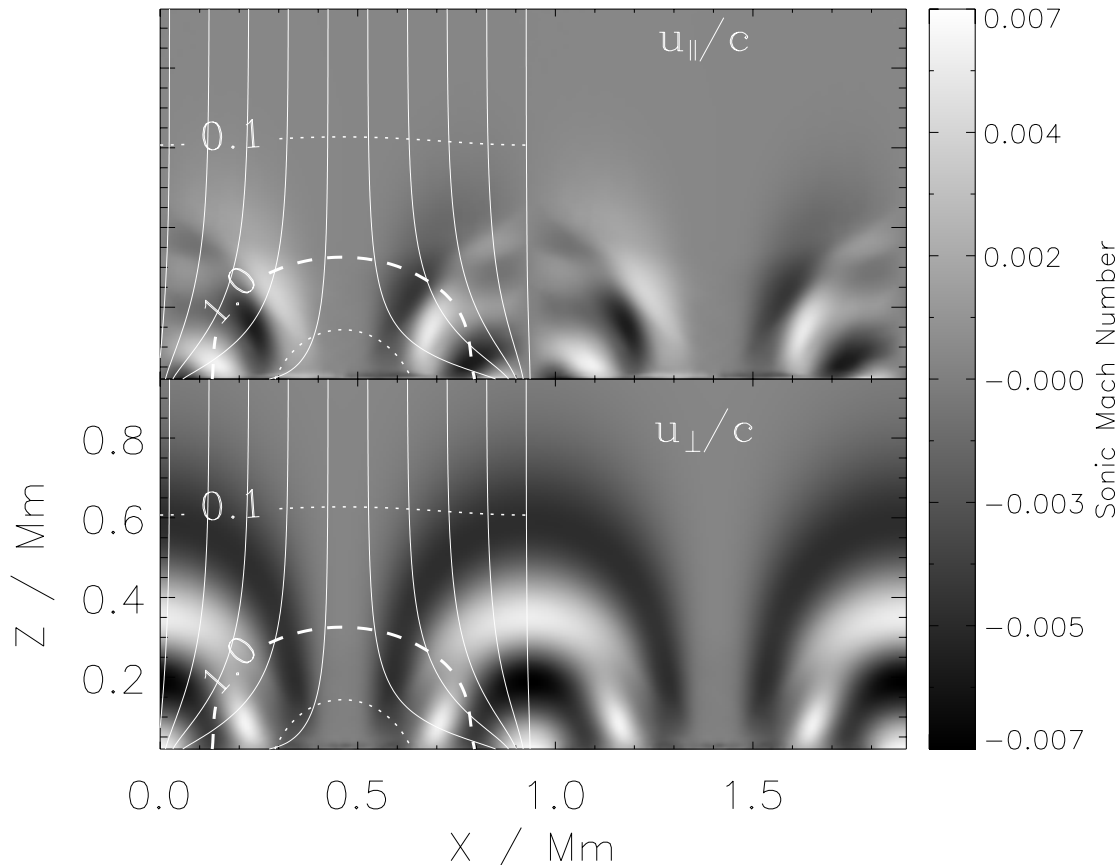

FIG. 1.—Snapshot showing velocity parallel (*top panel*) and transverse (*lower panel*) to the magnetic field in a simulation of waves in an open magnetic field configuration driven by shaking the lower boundary horizontally at 42 mHz. The velocity is shown as a fraction of the local sound speed. The snapshot is taken at 40 s of simulated time. Two horizontal periods of the computational domain are shown.
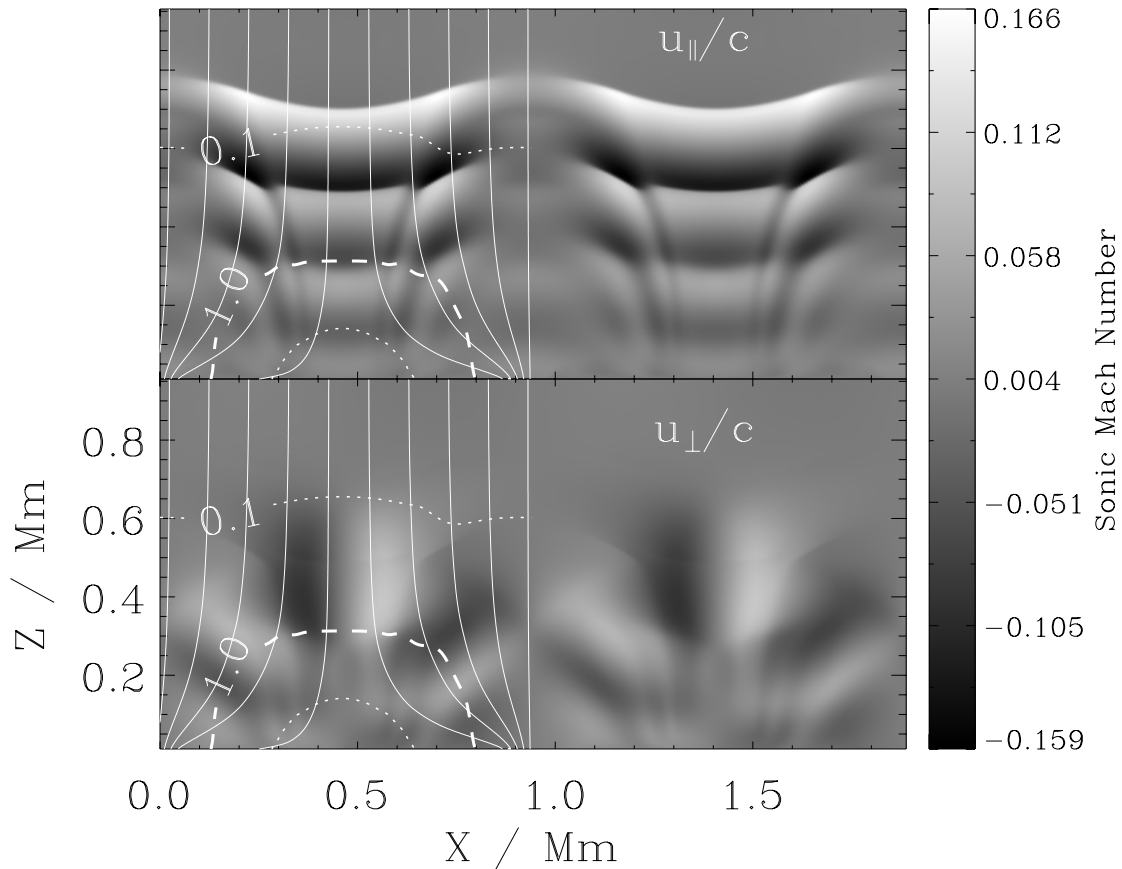
FIG. 2.—Same as Fig. 1, but for a case where the lower boundary oscillates in a vertical direction (simulated time 80 s)

ity for the boundary motion of 0.2 km s^{-1}, corresponding to a sonic Mach number of 0.024. For the transverse-driving case the amplitude of the motion is 0.1 km s^{-1} for the unipolar model and 0.35 km s^{-1} for the mixed-polarity model. (As we discuss below, in the transverse-driving cases the sonic Mach number remains much less than unity throughout the computational domain, so the amplitude of the driving affects the result only through a linear scaling.)

Each of Figures 1, 2, 4, and 5 comprises two panels: the upper panel gives a gray-scale rendering of the component of the instantaneous fluid velocity that is aligned with the instantaneous magnetic field, the lower gives the remaining component. The computational domain is reproduced twice in each panel to allow one to visualize the wave motions from network or internetwork perspectives. The white lines overplotted on the left half of the figures show the instantaneous locations of selected magnetic field lines as unbroken curves, and surfaces of constant values of the plasma β as labeled broken lines. The same curves apply to the right half of each figure but are omitted for clarity. Finally, we mention that the spatial coordinate is measured in megameters, and the gray scale is the instantaneous Mach number. As a complement to these snapshots, Figures 3 and 6 show the temporal development of the solutions corresponding to Figures 2 and 5, respectively. For these two figures, the gray scale shows the horizontal (*left panels*) and vertical (*right panels*) components of velocity multiplied by the square root of the local instantaneous density, to provide a quantity that is dimensionally the square root of an energy density.

The lower panels of Figures 1 and 4 show very clearly the propagation of the transverse (to **B**) oscillations up and outward along the flaring magnetic field of the dominant polarity network flux concentrations. Notice the rapid increase of the wavelength with height, which is a consequence of the (nearly) exponential increase of the Alfvén speed with altitude. This is brought about by the exponential decrease of the density, with the expansion of the magnetic field playing only a minor mitigating role. A careful comparison of Figure 1 with Figure 4 shows that the transverse waves in the mixed polarity equilibrium are about 75 km ahead of their counterparts in the unipolar equilibrium. This is explained by the greater magnetic field strengths present in the mixed polarity equilibrium network. For later comparison, we note that the constant-β surfaces are nearly indistinguishable from their initial locations.

As the core of the network magnetic field resides entirely in a low-β plasma, these crescent-shaped waves are *fast* MA waves, as evidenced by the fact that the motions are generally transverse to the magnetic field, with little compressional density fluctuation. The propagation speed and the spatial wavelengths are tied to the fast speed: $(a^2 + c^2)^{1/2} \approx a$.

Another piece of support for this identification comes from the striking difference between the lateral spatial variation of the waves at the top and the bottom of the atmosphere. Near the top of the atmosphere, the crescents from the distinct flux concentrations merge in such a manner that the *entire* uniformly magnetized atmosphere moves left and right en masse. This mimics the forcing at the

$$\rho^{1/2}\, u\, /\, (J\ m^{-3})^{1/2}$$

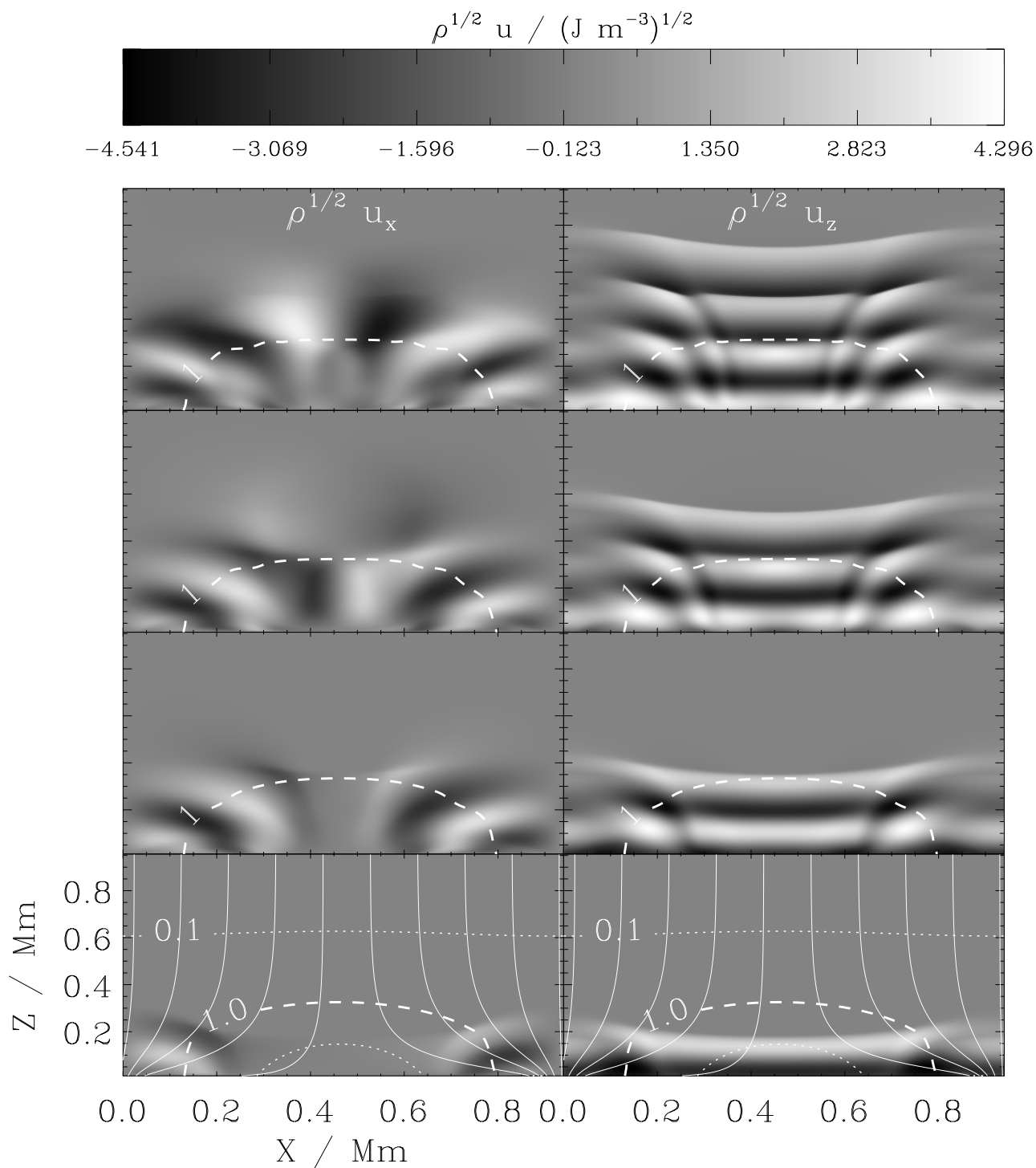| −4.541 | −3.069 | −1.596 | −0.123 | 1.350 | 2.823 | 4.296 |

FIG. 3.—Time sequence of the development of the simulation shown in the previous figure, showing the horizontal (*left panels*) and vertical (*right panels*) velocities multiplied, in each case, by the square root of the density. The snapshots correspond to simulated times of 20, 40, 60, and 80 s.

atmospheric base and has essentially zero horizontal wavenumber. The concentration of the magnetic field at the atmospheric base creates motions with higher order horizontal wavenumbers, despite the forcing at wavenumber zero. It is well known from the analysis of waves in uniformly magnetized isothermal atmospheres that the vertically propagating fast MA wave is completely reflected from a layer where its lateral phase velocity ω/k matches the local fast speed. Clearly, the horizontal phase speed of the wavenumber zero component is infinite, and so this component cannot be reflected. The wavenumber one component, based on the 1 Mm lateral extent of our computational domain and the 42 mHz driving frequency, has a horizontal phase speed of 42 km s^{-1}. Higher wavenumber components obviously have proportionately smaller horizontal phase speeds. The Alfvén speed at the top of the atmosphere is comfortably in excess of this value for both equilibria, in agreement with the observation that only the zero wavenumber component is making it to the top of the simulation.
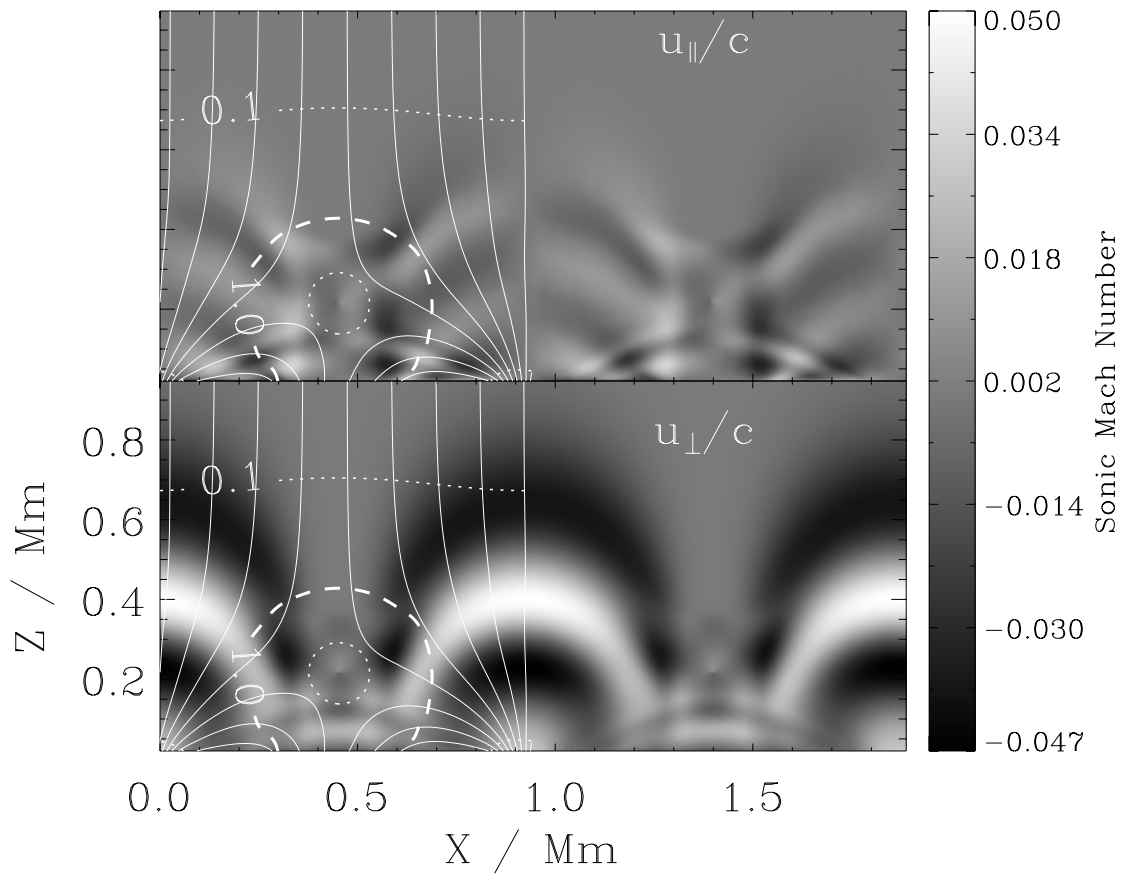
Fig. 4.—Same as Fig. 1, but for a mixed-polarity (X-point) geometry (simulated time 40 s)
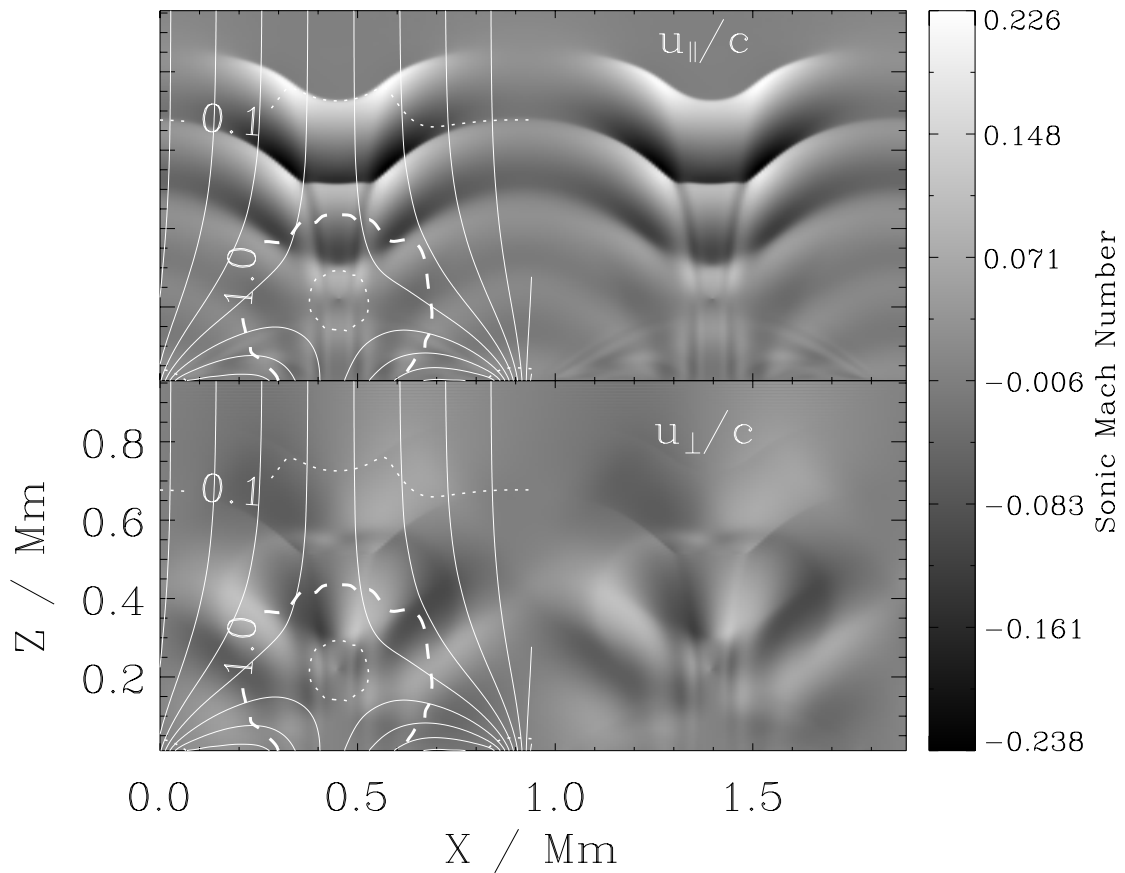

Fig. 5.—Same as Fig. 2, but for a mixed-polarity (X-point) geometry (simulated time 80 s)

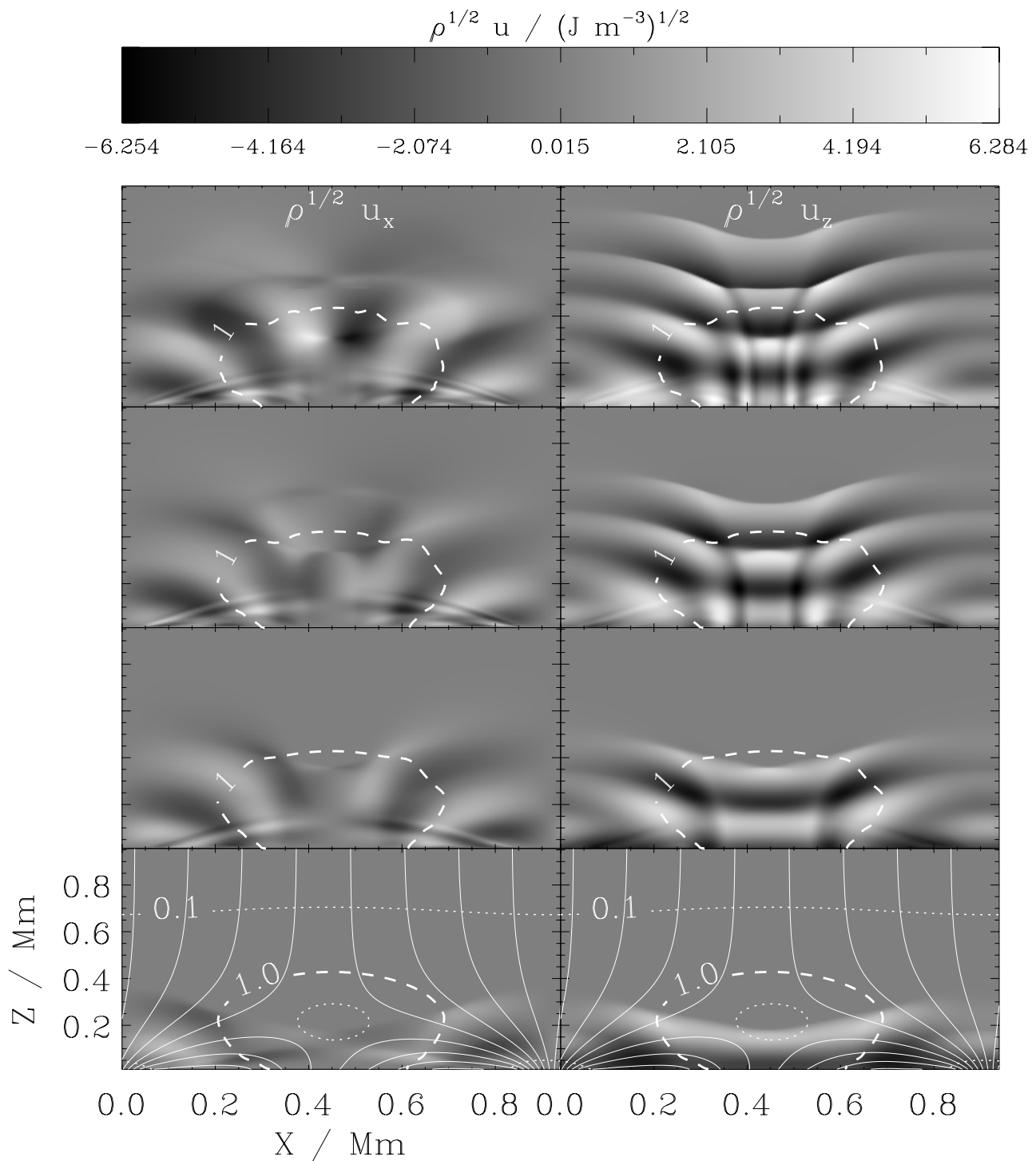$$\rho^{1/2} \, u \; / \; (J \; m^{-3})^{1/2}$$

FIG. 6.—Same as Fig. 3, but for a mixed polarity (X-point) geometry

If we continue to focus on Figures 1 and 4 but turn our attention to the upper panels, we see a clear signature of the presence of the slow MA wave. The region between $x = 0.7$ and $x = 1.2$ Mm in the upper panel of Figure 4 provides the best evidence. One observes a herringbone pattern of vertically stacked chevrons. Note in particular the *anti*symmetry about the vertical magnetic field line that marks the center of the network flux concentration. The chevrons have a constant vertical extent that is smaller than that exhibited by the crescents present in the lower panel. The motions associated with these waves are field-aligned (they are

absent in the lower panel), and they propagate at the sound speed. Hence, they are readily identified as slow MA waves in the low-β plasma of the network interior.

One may well ask why the slow MA herringbone pattern is more obvious in Figure 4 than in Figure 1 and, in particular, why it is broader in horizontal extent. We noted above that the slow MA wave is a direct by-product of the transverse forcing. Near the core of the network, the slow MA wave is generated in a low-β plasma and is guided along the magnetic field lines through low-β plasma. Hence, it has no opportunity to change its character or interact with the fast

MA waves present in the lower panel(s). As we move outward from core of the network the magnetic lines of force become more inclined, but of greater importance is that they eventually pass through atmospheric layers where the plasma β is of order unity or greater. Recall from § 3.2 that mode mixing between fast and slow MA waves occur in these layers, so the slow MA waves generated at the low-β base of the edges of the network suffer reflection and conversions that their network core counterparts do not. The reason for the different lateral extents of the slow MA herringbone patterns between 1 and 4 is now clear if we estimate the outermost network magnetic line of force that manages to avoid passing through a $\beta \approx 1$ mixing zone!

Slow MA waves of the high plasma-β variety are also present but only in the mixed polarity case (Fig. 4). The transverse motion of the entire lower boundary also generates transverse (to $\boldsymbol{B}$) waves that propagate up the reverse-polarity flux concentration. Here the base value of the plasma β is greater than 1, and moreover, it is an *increasing* function of altitude immediately above the minority flux slab.[9] As the lower panel of Figure 4 confirms, high-β slow MA waves have displacements transverse to the prevailing magnetic field. They are also guided along the magnetic field. Thus, as they propagate upward from the weak-field flux concentration, their propagation speed decreases, as does their wavelength, and they are diverted sideways and then downward. In so doing, they run head-on into different waves that were generated on the extreme closed-field flanks of the dominant polarity flux concentrations and have suffered complicated modifications in making their passage through the $\beta \approx 1$ circle.[10]

The closed-field region of Figure 4 (and Fig. 5) is complicated both because of the X-point present in the equilibrium magnetic field but also because there is no clear domination of plasma or magnetic pressure throughout this zone. The fast and slow MA waves are not readily disentangled, even at such a high frequency as 42 mHz. The upper panel of Figure 4 demonstrates that there are field-aligned motions that are comparable in magnitude to the transverse motions we associated with the slow MA wave. Examination of time series provide a general impression that the semicircular separatrix that connects the dominant polarity network with the magnetic X-point effectively circumscribes, or perhaps contains, the complicated mixed-mode region, and that little coherent signal manages to cross the separatrix and enter the overlying open-field regions. Some information may manage to escape in this fashion, but it is visually, and presumably energetically, overwhelmed by the waves propagating upward along the open field network.

To complete our basic assessment of this quartet of elementary examples, we take up the radial driving cases of Figures 2 and 5. The upper panels of these figures show the slow MA wave propagating upward along the magnetic lines of force. The fronts are not parallel to the lower boundary, but their lateral variations reflect the fact that they have passed through regions where the magnetic field has sensible horizontal components and where the Alfvén

and sound speeds have been comparable. It is interesting to note how the instantaneous contours of the plasma β respond to the passage of the wave fronts! This occurs because of the large density and pressure fluctuations that accompany the wave steepening.

That the wave fronts are steepening with increasing altitude can be verified in three distinct ways. First, the color bars indicate that the Mach numbers are significant. Second, the waves themselves are significantly distorted from a pure sinusoid (compare this with the upper panels of Figs. 1 and 4). Third, the uppermost of the three wavefronts has a larger vertical extent than those which follow it. Examination of the field lines in the vicinity of the shocks in Figure 2 does not show any obvious change in the field direction across the shock front. However, enlarged plots of the magnitude of the field components across the fronts do show small jumps in the field, and the sign of these jumps is such as to move the field direction closer to the normal to the shock front—exactly as would be expected for a slow MHD shock, formed from the steepening of an MHD slow mode. However, the jumps in the magnetic field are small (typically much less than 1% in these calculations). Note that this steepening behavior occurs only for the slow modes. The fast-mode propagation speed increases very rapidly with height so the fast modes never have a chance to become nonlinear.

The slight retardation of the wave front over the internetwork reflects the presence of significant transverse magnetic fields that are present at the atmospheric base on the flanks of the dominant polarity network. The vertical compression of these horizontal magnetic fields acts to speed up the wave front as they move through this region. Thus, they gain slightly on the front that is moving up through the internetwork. The differential gain is more pronounced in the mixed-polarity case because the transverse fields are stronger than in the unipolar case. A comparison of Figures 2 and 5 show that the wave front in the mixed-polarity case is everywhere ahead of that in the unipolar case. In the flanks of the network, the stronger transverse field is the cause. Down the center of the internetwork, the greater degree of steepening (Mach number of 0.226 vs. 0.166) is the culprit.

In both Figures 2 and 5 the variation in the amount of steepening as one moves along the wavefront is significant. In each case, the wave steepens most in the internetwork region near the center of the computational domain where it propagates at all heights as an acoustic disturbance. In the neighboring regions, where the magnetic field is inclined to the vertical, the enhanced wave propagation velocity reduces the effective magnetoacoustic Mach number and hence suppresses the steepening of the wavefronts with height. We can anticipate that in solar applications this effect could cause significant variations in the visibility of chromospheric intensity oscillations above regions of inclined magnetic field.

At the center of the open field component there is no velocity enhancement from the inclined fields. In this region (between $x = 0.8$ and 1.1 Mm on the upper panel of Fig. 2) we see purely acoustic (slow mode) wave fronts that travel upward at the sound speed and are therefore nearly in phase with the waves in the center of the internetwork where the field is also vertical (the wave over the internetwork leads slightly because of its nonlinearity). These slow waves are more clearly visible in Figure 3, on the

---

[9] This should be contrasted with the situation in the dominant polarity surrounding network!

[10] The absence of this behavior in Fig. 1 stems from the lack of appreciable vertical magnetic field threading the boundary between the unipolar flux concentrations. Only a viscous boundary layer can mediate the coupling to the overlying magnetic field. Clearly this is not particular efficient in the present circumstances.

right-hand side panels for $x > 0.8$ Mm. In the corresponding regions in Figures 5 and 6 the slow wave fronts are not clearly visible. In this case, the accumulated phase difference between the waves over the neutral point and the accelerated waves that propagate through the closed-field component is very close to a whole wave period so that the slow-mode component rises apparently in phase with the fast component, giving rise to the illusion of wave fronts that are continuous across the network component. In fact, the slow component is almost exactly one period behind the fast component, which is why the first wave front in the upper panel of Figure 5 vanishes there but the following wave fronts all appear continuous. A comparison of the waves at the far right-hand side edges of Figures 3 and 6 shows that they are, indeed, traveling at the same phase speed.

The lower panels of Figures 2 and 5 show the signature of the associated fast MA wave. The analysis proceeds essentially along the lines stated above when we tackled the slow MA wave in the transverse driving examples of Figures 1 and 4 but is subject to the appropriate reverse substitutions. The obliquity of the magnetic field causes a slight amount of fast MA wave to be generated in the flux concentrations with radial driving. The sense is again antisymmetric across the central vertical field line. A herringbone chevron pattern is once more anticipated and is indeed evident in the lower panels of Figures 2 and 5.

However, owing to the nontrivial variation of the Alfvén speed across the expanding network flux, the chevrons develop curvature and the vertical extent of the chevrons increases rapidly with altitude. Their merger near the top of the atmosphere is accomplished in the sense that only the wavenumber zero component is allowed to pass through this boundary, consistent with the magnetic Lamb criterion. The same arguments advanced before regarding the lateral extent of the network magnetic field lines that do not encounter $\beta \approx 1$ conversion zones, and the pattern visibility, basically remains in force.

5. INTERNETWORK OSCILLATIONS

As an example of the application of these ideas to a real solar problem we now consider the effect of relatively weak fields on oscillations in the internetwork. Figure 7 shows a model configuration for the field of a piece of magnetic network. It is a simple monopolar flux sheet, but in contrast to Figure 1 the flux tube is now surrounded at the photospheric level by a much larger field-free region. We have also extended the computational domain upward to 16 scale heights. Note that although the field lines spread out rather slowly with height, the contours of plasma β spread quite rapidly so that the $\beta = 1$ contour forms a continuous surface varying in height between 0.8 and 1.6 Mm above the photosphere. The computational domain consists of 200 points in the horizontal and 92 in the vertical. The velocity amplitude of the piston is 3.7% of the sound speed.

We consider first the effect of the field on internetwork oscillations by driving the system with a piston confined to the region outside the network element. Figure 8 shows the velocities transverse and parallel to the magnetic field, while Figure 9 shows the horizontal and vertical velocities scaled with the square root of the density. (The domain of the numerical calculations corresponds to the whole structure shown in Figure 7, while Figures 8 and 9 show only expanded views of the region where the velocity departs signifi-
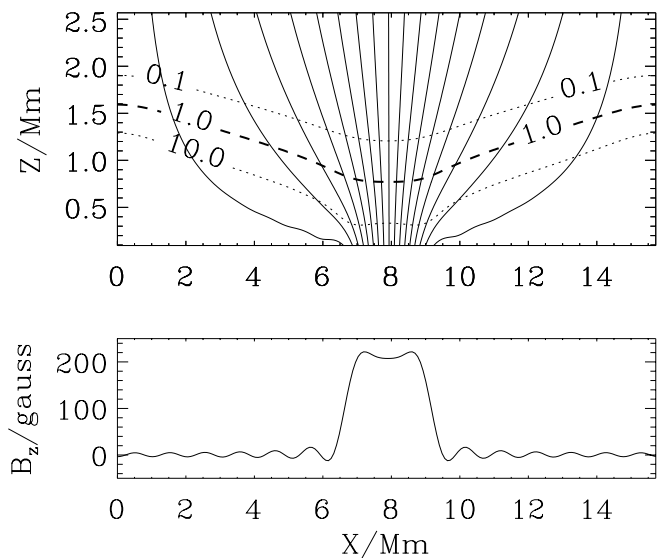

FIG. 7.—Field configuration corresponding to a network element and the surrounding internetwork. Note that the upper panel is plotted with an expanded vertical scale, and therefore the apparent slopes of the field lines and β contours may be misleading.

cantly from zero. They have been plotted with an aspect ratio very close to unity so that the slopes of the magnetic field lines and β-contours are not misleading.)

As the wave travels upward from the source its velocity is initially close to radial. However, as it approaches the $\beta = 1$ layer, the wave front tilts and the velocity acquires a significant horizontal component. The tilt of the wave front is much as one would expect from a simple physical-optics picture. The parts of the wave front closer to the flux tube experience an extra restoring force owing to the Lorentz forces, thus accelerating that part of the front ahead of the part farther from the flux concentration. The tilting of the wave front then causes the direction of the propagation to tilt, as the propagation direction is locally along the normal to the wave fronts. Because of the unlimited increase of the Alfvén speed with height, the wave front is eventually turned around until it is propagating back downward again, in a manner analogous to the phenomenon of total internal reflection in optics (or the reflection of nonradial p-modes by the increasing sound speed in the solar interior). In the region above the reflecting surface the wave is still present as a pattern of long evanescent tails showing horizontal propagation in the direction away from the flux element.

Examination of Figure 8 shows that as the wave travels into the low-β region, the velocity vector becomes oriented so that it is predominantly in a direction transverse to the magnetic field. Thus, the wave, which starts out as a fast (acoustic) mode in the high-β region near the piston remains a fast wave as it propagates into the low-β region, and the total reflection discussed in the previous paragraph can therefore be viewed as a consequence of the rapid increase of the fast magnetosonic speed with height, coupled with the significantly nonzero propagation angle between the initial wavevector and the gradient of that wave speed.

These simulations show a number of features that may be relevant to observations of internetwork waves. Carlsson & Stein (1997) showed that the K grain phenomenon could be accurately modeled in terms of upwardly propagating
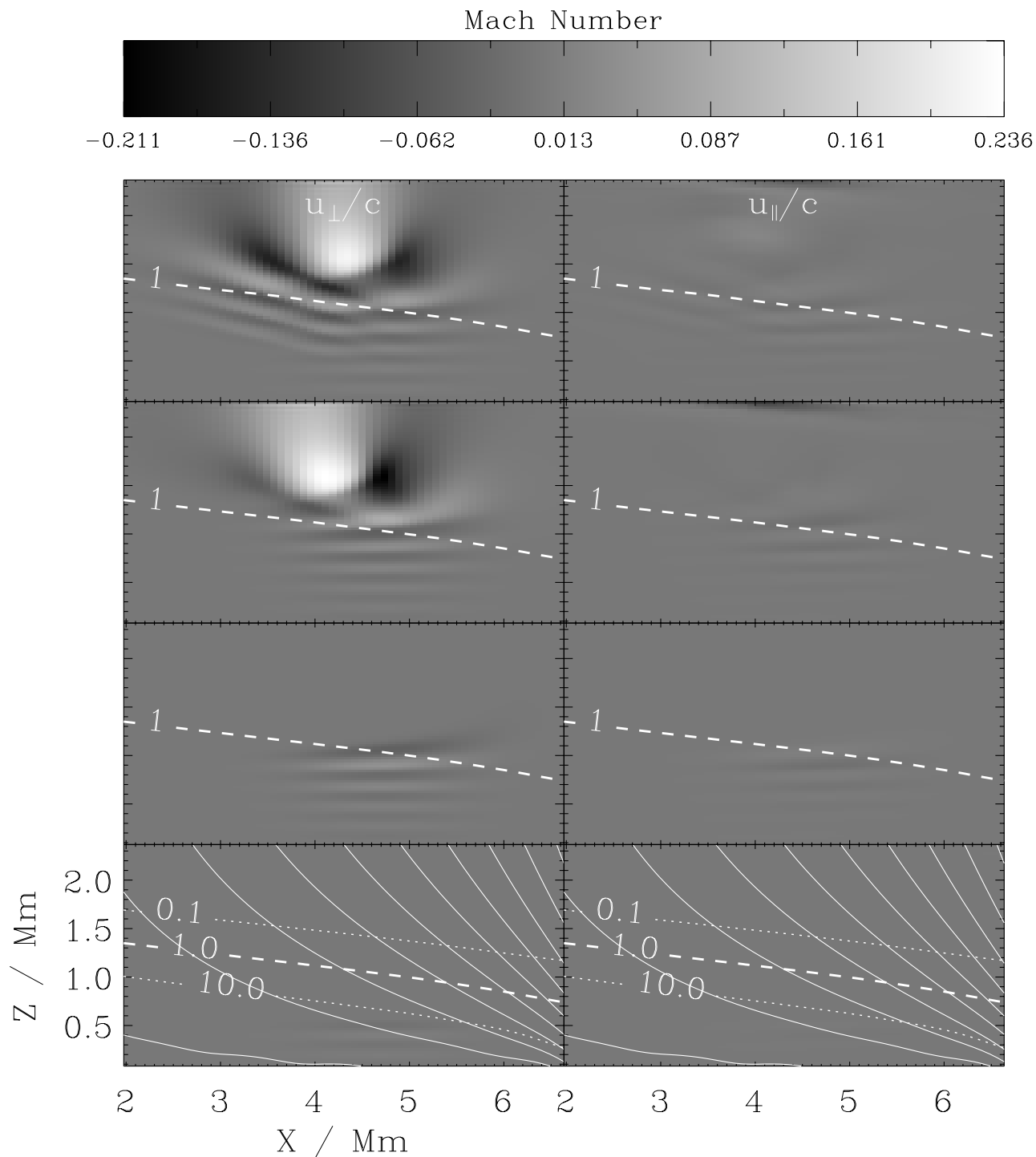
FIG. 8.—Results of a simulation of an oscillation driven through the geometry of Fig. 7 by a vertically moving piston located in the internetwork region. The left panels show the velocity component transverse to the field, and the right panels are the component parallel to the field, normalized to the sound speed in each case. The four snapshots correspond to times 55, 110, 155, and 220 s after the piston is switched on. The frequency is 42 mHz. For reference, contours of plasma β and magnetic field lines are shown in the lower panels, and the $\beta = 1$ contour is shown in all panels.

acoustic shocks in an unmagnetized medium. Here we find that the introduction of an inhomogeneous magnetic field leads to reflection, interference between upwardly and downwardly propagating waves, and hence to rapid (supersonic) horizontal phase propagation, as seen in observations of internetwork oscillations.

The reflecting layer in this calculation is a corrugated surface and in the real solar atmosphere the contours of constant β will be even more irregular. If we assume that the height of formation of the spectral diagnostic in which the waves are measured varies much less than the height of the β contours, then we can expect that a diagnostic that is formed below the reflecting layer in some regions of the Sun will be formed above it in others and that in those regions the measured amplitude will be very small. This seems a promising explanation for the observed intermittancy of

$$\rho^{1/2} \, u \; / \; (J \; m^{-3})^{1/2}$$

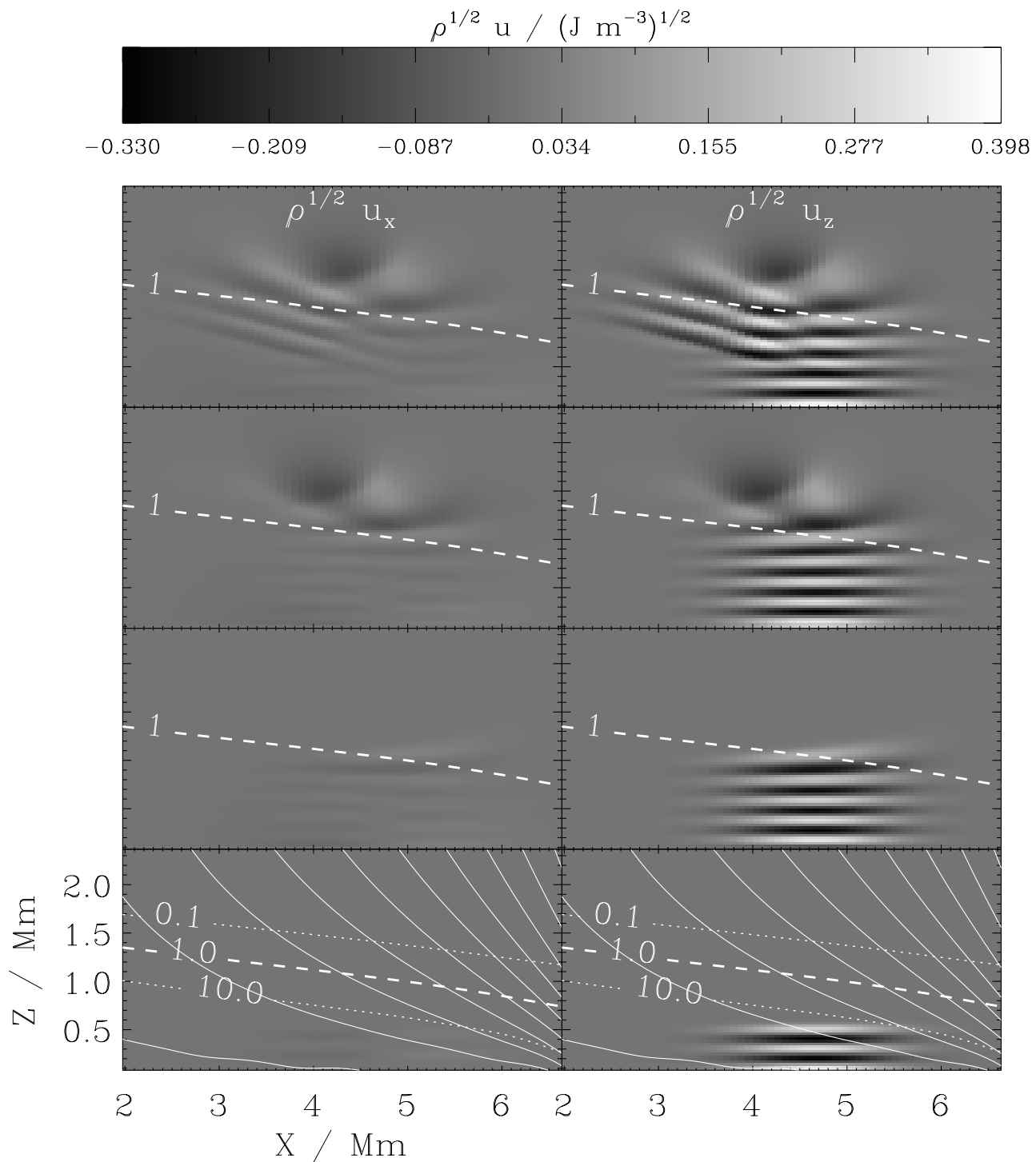−0.330   −0.209   −0.087   0.034   0.155   0.277   0.398

FIG. 9.—Results for the same calculation as Fig. 8, but showing the horizontal (*left panels*) and vertical (*right panels*) velocities multiplied, in each case, by the square root of the density.

internetwork waves (e.g., Carlsson 1999; Judge, Tarbell, & Wilhelm 2001), particularly in view of the correlation between the intermittancy and the magnetic field shown by McIntosh et al. (2001) and Mcintosh & Judge (2001).

6. NETWORK OSCILLATIONS

Figures 10 and 11 show comparable results for the case where the piston is confined to the interior of the network element. The contrast with the previous case is striking. As the wave enters the low-β region, the field-aligned com-

ponent of velocity remains dominant, characteristic of an MHD slow mode. In this case, where the direction of the wavevector is also close to that of the magnetic field, the slow mode is essentially a pure acoustic oscillation, guided by the magnetic field and traveling at the sound speed. As it propagates upward it will therefore steepen like an ordinary nonlinear sound wave but will not, in an isothermal model such as this, be reflected. The amplitude of this compressive component is somewhat smaller in this calculation than in the previous, internetwork case. At a height of 1 Mm, the
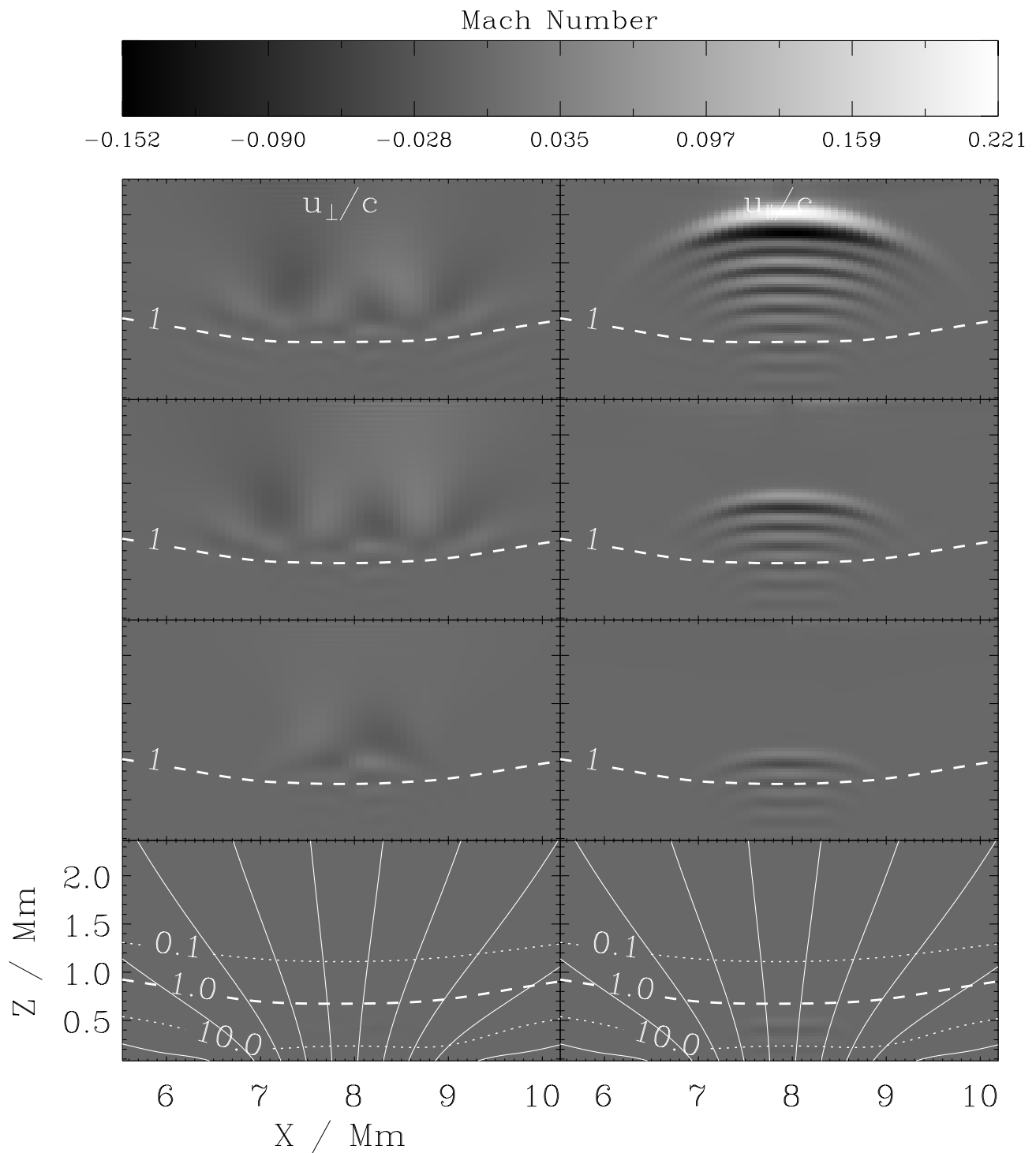
FIG. 10.—Same as Fig. 8, but now with the piston located wholly inside the network element

wave amplitude in this case has grown by a factor of ~ 8 relative to the amplitude of the piston, while in the previous calculation the growth factor at the same height is ~ 9.5. The smearing of the wave front by the spreading magnetic field seems to be responsible for the difference.

The physical picture of the waves in Figures 10 and 11 is therefore that they are predominantly acoustic oscillations everywhere, and that as they move into the strong-field low-β region they become guided along the field lines. Mathematically, however, this means that waves that start

out as fast modes have now become slow modes, even though there has been no change in the restoring force determining their physical character. This is in contrast to the case discussed in § 4 above, where the waves remained "fast" everywhere but the principal restoring force switched from gas pressure to Lorentz forces as the wave traveled from the high-β to low-β region. This raises two questions: (1) which, if either, of these two calculations involves something which can be described as "mode conversion"? and (2) why are the two calculations so different?
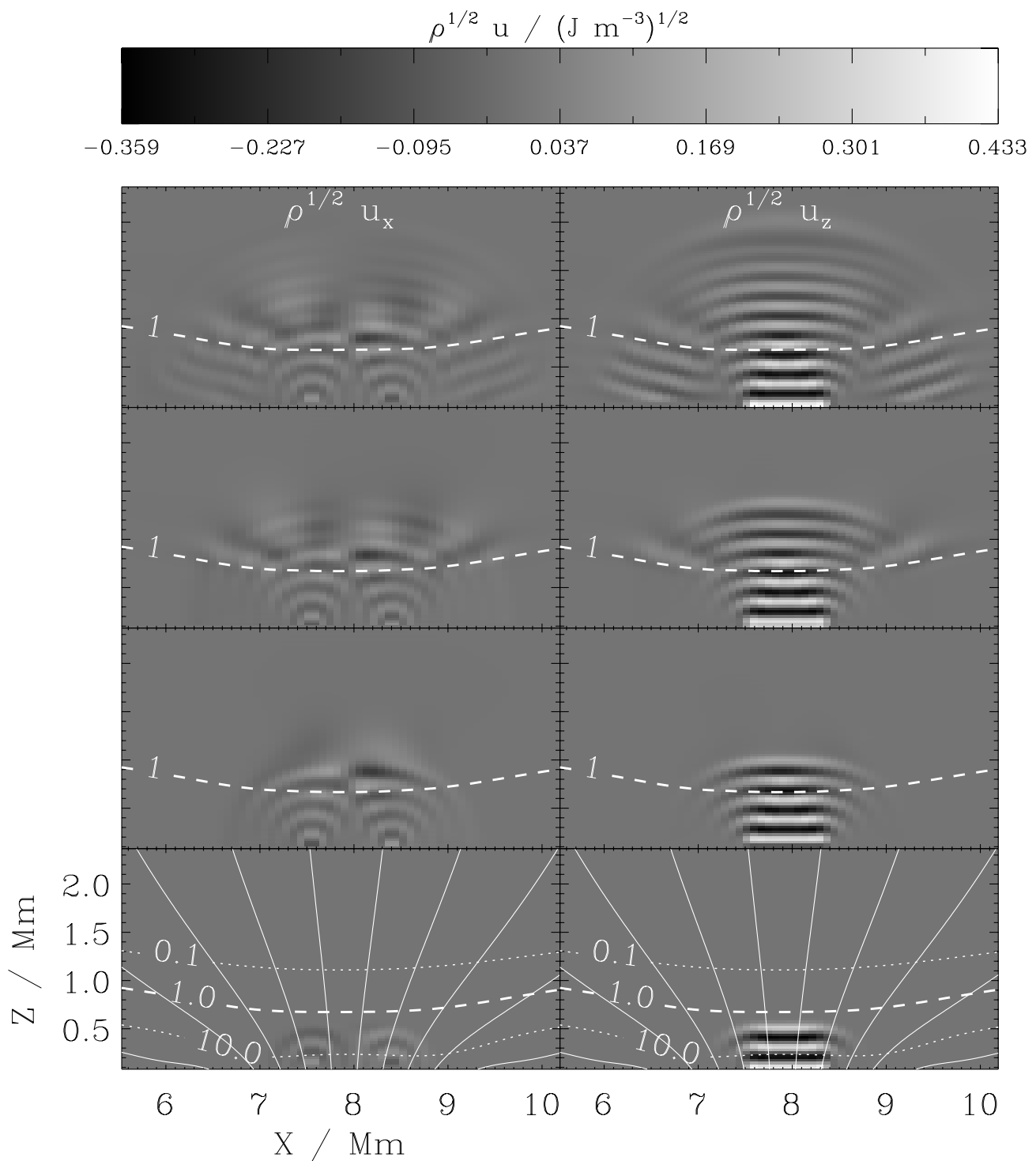
Fig. 11.—Same as Fig. 9, but with the piston located wholly inside the network element

We believe that the first of these questions involves principally issues of semantics, and we therefore prefer to eschew the terminology of "mode conversion" entirely. The second, however, is a real physical and mathematical question and cannot be brushed aside. The answer seems to lie in the degeneracy that occurs (in the case of a uniform field in a homogeneous atmosphere) when the wavevector lies parallel to the field and the sound speed and Alfvén speed are equal. In this case the slow and fast modes are perfectly degenerate. Thus, the "fast" acoustic wave propagating up

the flux concentration through $\beta = 1$ is able to couple perfectly to the "slow" acoustic wave that propagates up into the low-β region. In the internetwork case of § 5, by contrast, the angle between the wavevector and the magnetic field is close to 45°, and no such coupling is possible. The wave therefore remains "fast" everywhere and so is reflected.

From the solar point of view, the principle problem of interpretation of Figures 10 and 11 is that such waves are not observed in magnetic network elements in the Sun.

Among the possible explanations for this observation are the following:

1. The waves are present, but the attenuation of the wave amplitude in the low-β region masks their visibility. Attenuation by spreading of the wave front along the diverging field lines will be greater in three dimensions than in these two-dimensional calculations. There is also a small, but possibly significant, coupling to the low-β fast modes that will also remove power from the upwardly propagating slow waves.

2. There are no wave sources in network regions.

3. The higher temperature and density scale height within the network suppresses the growth of wave amplitude with height.

4. The complex magnetic field geometry in the network leads to efficient mode conversion and dissipation.

5. The waves are present but dissipated by Pedersen currents (Goodman 2000), possibly leading to heating of the network elements.

The model used here does not contain enough of the relevant physical complexity to allow us to choose between these possibilities. In the future we hope to build network models incorporating complex, tangled, nonpotential fields in order to test, by direct simulation, the viability of some of these possibilities.

7. CONCLUSIONS

The theoretical study of magnetoacoustic oscillations in the magnetized solar atmosphere has, up to the present time, been largely confined to systems in which all variation in the medium has been in a single spatial direction. Evidently, such models can only be a crude approximation to the true complex dynamics of the highly three-dimensional solar atmosphere. In this paper we have gone beyond these one-dimensional models by introducing two-dimensional magnetic fields, while retaining as much simplicity as possible in the remaining physics—one-dimensional thermodynamic stratification, perfect nonradiating isothermal gas, potential magnetic field, plane-parallel geometry, etc.

However, even with these physical simplifications we have gained access to a very rich phenomenology of wave processes. Among these, the most important consequences for solar studies seem to arise from the effect of inclined magnetic fields on the propagation of compressive, longitudinal, acoustic-like waves. The additional Lorentz restoring forces (magnetic pressure and tension) are typically very small relative to the gas pressure at the photosphere, but their ratio rises exponentially with height. In geometries such as those of § 4, the effect of this additional force is to increase the wave propagation speed and hence to suppress the steepening and shocking we would otherwise expect from an acoustic disturbance.

In cases such as the internetwork simulation of § 5, where the field remains significantly nonvertical for many scale heights, the effect is ultimately to reflect all or almost all the wave energy back downward. The height of this reflecting layer will depend on the field geometry and wave frequency, but in the Sun it will certainly be a highly complicated surface, and this strongly varying reflection height may be responsible for the intermittancy seen in the oscillations.

In order to test this hypothesis we need to study wave propagation in more realistic atmospheres where we can make reasonably confident statements about the height sensitivity of the spectral diagnostics in which the observations are made. A not unreasonable goal is to use observed photospheric fields as the foot points of a potential field extrapolation and then to use measured photospheric velocities as a piston to drive waves through this system using the numerical techniques employed here. With simultaneous chromospheric observations we could then make a direct comparison between simulated and observed wave fields.

More speculatively, the downwardly propagating waves must eventually be reflected back upward again by the increasing temperature below the solar surface. The entire system should therefore operate as a resonant cavity but one with, presumably, chaotic ray paths and nonlinear dissipative waves. Understanding the properties of waves in such a system will pose an interesting challenge for modelers.

REFERENCES

Adam, J. A. 1981, Ap&SS, 78, 293
———. 1986, Ap&SS, 127, 163
———. 1989, J. Math. Phys., 30, 744
———. 1990, Wave Motion, 12, 385
Banerjee, D., Hasan, S. S., & Christensen-Dalsgaard, J. 1995, ApJ, 451, 825
Barnes, A. 1992, J. Geophys. Res., 97, 12105
Bazer, J., & Hurley, J. 1963, J. Geophys. Res., 68, 209
Biermann, L. 1948, Z. Astrophys., 25, 161
Bogdan, T. J., & Cally, P. S. 1997, Proc. R. Soc. London A, 453, 943
Čadež, V. M., Oliver, R., & Ballester, J. L. 1996, A&A, 314, 636
Cally, P. S. 1984, A&A, 136, 121
———. 2001, ApJ, 548, 473
Campos, L. M. B. C., & Saldanha, R. 1991, Geophys. Astrophys. Fluid Dyn., 56, 237
Cargill, P. J., Spicer, D. S., & Zalesak, S. T. 1997, ApJ, 488, 854
Carlsson, M. 1999, in 9th European Meeting on Solar Physics: Magnetic Fields and Solar Processes, ed. A. Wilson (ESA SP-448; Noordwijk: ESA), 183
Carlsson, M., & Stein, R. F. 1997, ApJ, 481, 500
Cross, R. C. 1988a, Plasma Phys. Controlled Fusion, 30, 1213
———. 1988b, Planet. Space Sci., 36, 1461

Dai, W., & Woodward, P. R. 1998, ApJ, 494, 317
Dorch, S. B. F., & Nordlund, Å. 1998, A&A, 338, 329
Dungey, J. W. 1969, in Physics of Geomagnetic Phenomena, Volume II, ed. S. Matsushita & W. H. Campbell (New York: Academic Press), 913
Ferraro, C. A., & Plumpton, C. 1958, ApJ, 127, 459
Goodman, M. L. 2000, ApJ, 533, 501
Goossens, M., Poedts, S., & Hermans, D. 1985, Sol. Phys., 102, 51
Hasan, S. S., & Christensen-Dalsgaard, J. 1992, ApJ, 396, 311
Hollweg, J. V., & Lilliequist, C. G. 1978, J. Geophys. Res., 83, 2030
Hyman, J. 1979, in Advances in Computer Methods for Partial Differential Equations III, ed. R. Vichnevetsky & R. Stepleman (New Brunswick: IAMCS), 313
Judge, P. G., Tarbell, T. D., & Wilhelm, K. 2001, ApJ, in press
Kamp, L. P. J. 1989, Phys. Fluids B, 1, 1385
Korevaar, P. 1989, A&A, 226, 209
Leroy, B., & Schwartz, S. J. 1982, A&A, 112, 84
Lites, B. W., Rutten, R. J., & Kalkofen, W. 1993, ApJ, 414, 345
Mackay, D. H., & Galsgaard, K. 2001, Sol. Phys., 198, 289
McIntosh, S. W., et al. 2001, ApJ, 548, L237
Mcintosh, S. W., & Judge, P. G. 2001, ApJ, in press
McKenzie, J. F. 1973, J. Fluid Mech., 58, 709

Murata, H. 1986, J. Plasma Phys., 36, 243
Nye, A. H., & Thomas, J. H. 1976, ApJ, 204, 573
Oliver, R., Ballester, J. L., Hood, A. W., & Priest, E. R. 1993, ApJ, 409, 809
Orszag, S. A., & Tang, C. 1979, J. Fluid Mech., 90, 129
Osterbrock, D. E. 1961, ApJ, 134, 347
Pintér, B., Čadež, V. M., & Goossens, M. 1998, A&A, 332, 775
Pintér, B., & Goossens, M. 1999, A&A, 347, 321
Poedts, S., & Goossens, M. 1987, Sol. Phys., 109, 265
———. 1988, A&A, 198, 331
Poedts, S., Hermans, D., & Goossens, M. 1985, A&A, 151, 16
Rosenthal, C. S. 1990, Sol. Phys., 130, 313
Schwartz, S. J., & Bel, N. 1984, A&A, 137, 128
Schwarzschild, M. 1948, ApJ, 107, 1
Shibata, K. 1983, PASJ, 35, 263
Skartlien, R., Stein, R. F., & Nordlund, Å. 2000, ApJ, 541, 468
Sod, G. 1978, J. Comput. Phys., 27, 1
Thomas, J. H. 1982, ApJ, 262, 760
———. 1983, Annu. Rev. Fluid Mech., 15, 321
Thomas, J. H., & Scheuer, M. A. 1982, Sol. Phys., 79, 19

Thomas, R. N. 1948, ApJ, 108, 130
Tirry, W. J., & Goossens, M. 1995, J. Geophys. Res., 100, 23687
Tirry, W. J., Goossens, M., Pinter, B., Čadež, V., & Vanlommel, P. 1998,
    ApJ, 503, 422
Vanlommel, P., & Goossens, M. 1999, Sol. Phys., 187, 357
Weinberg, S. 1962, Phys. Rev., 126, 1899
Weymann, R., & Howard, R. 1958, ApJ, 128, 142
Wright, A. N. 1990, J. Plasma Phys., 44, 361
———. 1991, Geophys. Res. Lett., 18, 1951
———. 1992, J. Geophys. Res., 97, 6429
Wright, A. N., & Evans, N. W. 1991, J. Geophys. Res., 96, 209
Yeh, T. 1974, Phys. Fluids, 17, 2282
Yu, C. P. 1965, Phys. Fluids, 8, 650
Zhugzhda, I. D., & Dzhalilov, N. S. 1982, A&A, 112, 16
———. 1984a, A&A, 132, 45
Zhugzhda, Y. D., & Dzhalilov, N. S. 1984b, A&A, 132, 52
Zhukov, V. I. 1985, Sol. Phys., 98, 39
———. 1990, Ap&SS, 174, 173
———. 1997, Sol. Phys., 173, 15